



## Fall and break-up of viscous miscible drops in a Hele-Shaw cell

Clément Toupoint <sup>1</sup>, Sylvain Joubaud <sup>1,2,\*</sup> and Bruce R. Sutherland<sup>3,4</sup>

<sup>1</sup>*Univ Lyon, ENS de Lyon, Univ Claude Bernard, CNRS, Laboratoire de Physique, 69367 Lyon Cedex 07, France*

<sup>2</sup>*Institut Universitaire de France (IUF), 1 rue Descartes 75005 Paris, France*

<sup>3</sup>*Department of Physics, University of Alberta, Edmonton, AB, Canada T6G 2E3*

<sup>4</sup>*Department of Earth and Atmospheric Sciences, University of Alberta, Edmonton, AB, Canada T6G 2E3*



(Received 23 March 2021; accepted 17 September 2021; published 6 October 2021)

We investigate the fall in a Hele-Shaw cell of viscous miscible drops in a more viscous ambient fluid with negligible diffusivity compared to the kinematic viscosity of the fluids. We measure the drop shape, thickness, and velocity for various viscosity and density ratios. The elongation of the drops is found to increase quadratically with the ratio of the drop and ambient fluid viscosity. The thickness of the drop is shown to be approximately half the thickness of the gap of the Hele-Shaw cell. We develop a theoretical expression of the drop falling velocity, taking into account the elongation and thickness of the drop. This agrees well with observations after multiplying by an empirically determined constant. In some circumstances the drops break up, either because of defects advected downwards within the drop or by instability of the shape of the drop.

DOI: [10.1103/PhysRevFluids.6.103601](https://doi.org/10.1103/PhysRevFluids.6.103601)

### I. INTRODUCTION

The dynamics of drops moving in a confined medium is a topic spanning diverse applications, from large-scale industrial problematics such as enhanced oil recovery [1], commercial inkjet printing [2], and the use of droplets in microfluidics [3]. The question of the miscibility of the displacing fluid with the ambient fluid is especially relevant for enhanced oil recovery, where miscible displacements are proven to be more efficient than immiscible ones [4].

Several laboratory experiments have examined the shape and motion of drops and bubbles in a Hele-Shaw cell [5–13]. The Hele-Shaw cell has long been used as an analog of a porous medium because of the similarity between the equations of fluid motion between two parallel plates that are sufficiently close together and those of the fluid motion in a porous medium of the same permeability (see the discussion by Saffman and Taylor [5]). In addition to these mathematical similarities, Hele-Shaw cells allow the easy experimental observation of a variety of phenomena [6,14]. The apparently simple problem of determining the falling velocity of an immiscible drop in a Hele-Shaw cell proves to be nontrivial. The experimental investigation of immiscible drops by Eri and Okumura [8] revealed the existence of two different regimes of energy dissipation, occurring either in the film or within the drop. Yahashi *et al.* [10] later elaborated on this finding by building a scaling law for the separation between the two regimes depending on the relative molecular viscosity of the drop ( $\mu_d$ ) and ambient fluid ( $\mu_a$ ), the capillary length, and the cell gap width  $H$ . In a subsequent experimental study, Keiser *et al.* [11] characterized the influence of the film on the drop velocity for different  $\mu_d$  and  $H$ , with  $\mu_d > \mu_a$ . Several studies also examined the film thickness for drops in an external flow [9,12,15]. In particular, the experimental investigation by Shukla *et al.* [13] produced a complete

\*sylvain.joubaud@ens-lyon.fr

film thickness map for falling immiscible drops in a Hele-Shaw cell. Their experimental results also matched with the theoretical expression of the falling velocity obtained in previous work [16,17]. In particular, the thin liquid film present between the drop and the walls of the cell has been shown to have a significant impact on the dynamics of the drop. In contrast, this film has no significant influence on the motion of bubbles, with their rising velocity well predicted by theory [5,6].

The break-up of confined immiscible drops in a Hele-Shaw cell has been investigated in a series of theoretical and numerical studies by Gupta *et al.* [18–20]. They carried out a linear stability analysis of circular immiscible drops translating in a Hele-Shaw cell and found that initially circular drops were stable for small perturbations, regardless of the Bond number ( $Bo$ ), which compares gravitational to interfacial capillary forces. They found that the initial drop deformation led to break-up for  $Bo < 60$ . However, they found that initially deformed drops were more stable at higher Bond number, even in the case of strong initial deformations. They were able to predict qualitatively the evolution of the shape of stable and breaking up drops. They did not extend their study to drops with negligible surface tension ( $Bo \rightarrow \infty$ ).

In all the studies discussed so far, capillary forces were shown to play an important role on both the shape of the film and the dynamics of the immiscible drop. The dynamics of miscible drops is less well understood. Lajeunesse *et al.* [21,22] and Petitjeans *et al.* [23] studied experimentally the displacement of ambient fluid in a Hele-Shaw cell by a heavier, miscible one, injected from the top across the entire width of the cell. But few studies have examined a miscible drop.

In an unconfined medium it is known that miscible drops are unstable, tending to break-up into several smaller drops as they fall [24–28]. This break-up phenomenon is inhibited for immiscible drops [18,19,29] due to surface tension. A miscible spherical drop falling into a lighter fluid expands horizontally into a ring. This ring expands until it reaches a critical size, and breaks-up into smaller drops. In turn, it is possible that these smaller drops break up as well. This phenomenon has been observed for a long time [30] but is not yet fully understood. A series of experimental studies by Arecchi *et al.* [25,26], Residori *et al.* [27], and Arecchi *et al.* [31] found that the break-up occurred because of a competition between diffusive and viscous effects. More recent experimental and numerical investigations by Shimokawa *et al.* [28] and Shimokawa and Sakaguchi [32] highlighted the role of the Rayleigh-Taylor instability in the break-up of drops. In all these studies, the ring shape of drops breaking-up in an unconfined medium is intrinsically three-dimensional. It is therefore expected that the confinement will play an important role upon the drop stability. Garcimartín *et al.* [7] performed experiments with weakly confined quasispherical miscible drops falling in a Hele-Shaw cell for which the radius of the drop,  $R$ , was comparable to half the gap width,  $H$ . They also observed the break-up of the drop. They found that ambient fluid penetrated inside the drop, and that mixing ensued within the drop which triggered instability. Subsequently, they were able to satisfactorily scale the break-up time of the drop with a characteristic time  $\tau_i$  based on the drop radius and internal fluid velocity  $v_i$ , so that  $\tau_i = R/v_i$ .

Here we report upon experiments of highly confined, pancake-shaped drops ( $R \gg H$ ). The shape of the liquid film between the drop and the walls of the cell in our work is therefore very different from that of the experiments of Garcimartín *et al.* [7]. To the knowledge of the authors, a study of highly confined miscible drops has not previously been examined experimentally. Specifically, our experiments examine a falling miscible drop having lower viscosity than the ambient fluid. We focus on measurements of the falling velocity of the drop, and we use light absorption to measure the thickness of the drop. Finally, we examine the parameters leading to the break-up of the drop.

The paper is organized as follows. After presenting some theoretical considerations in Sec. II, we describe the experimental setup in Sec. III. We then present measurements of the shape, thickness, falling velocity, and stability of the drop in Sec. IV. Discussion and conclusions are given in Sec. V.

## II. THEORETICAL CONSIDERATIONS

In this section we present some theoretical considerations that will serve as a basis for the analysis of the experimental results. We consider a vertically oriented Hele-Shaw cell, as shown in Fig. 1.

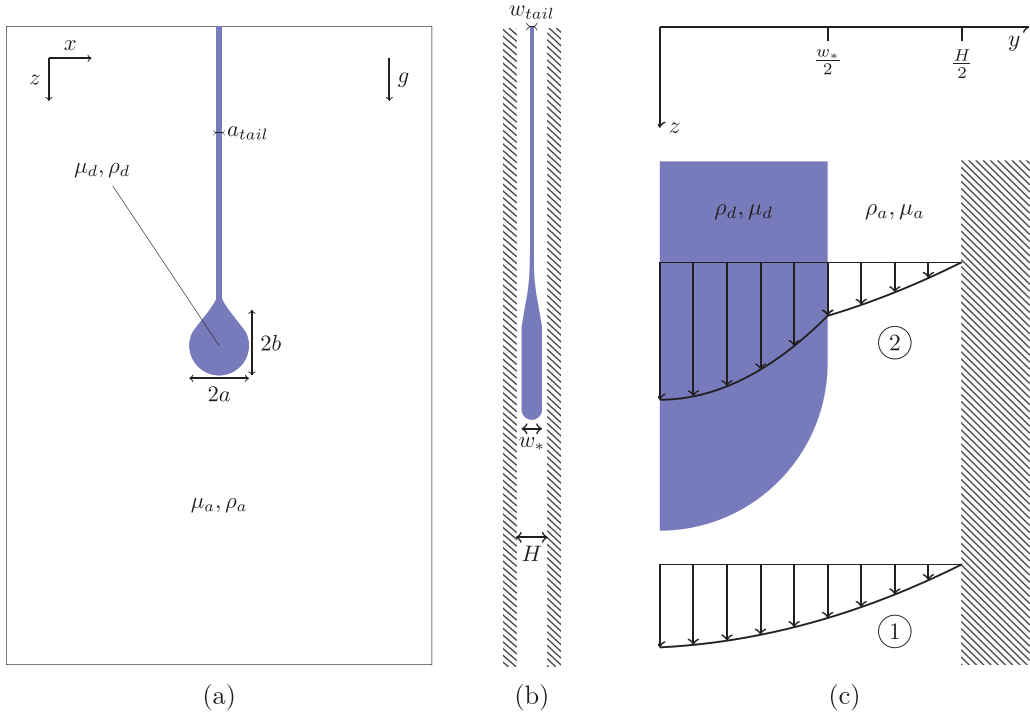


FIG. 1. Schematic view of a drop with a tail of fluid falling into the experimental cell (a)  $(x, z)$  and (b)  $(y, z)$  plane. (c) Sketch of the velocity profiles in the cross section of half the cell (in the  $(y, z)$  plane). We denote by a circled 1 an area of the cell far from the drop, and by a circled 2 an area between the drops and the walls.

We denote by  $(x, z)$  the plane of the cell, where the  $x$ -axis is horizontal and the  $z$ -axis is vertical downwards. The  $y$ -axis is orthogonal to the walls of the cell, and its origin is in the middle of the gap. We consider a drop of width  $2a$  (along the  $x$ -axis), height  $2b$  (along the  $z$ -axis), density  $\rho_d$ , and molecular viscosity  $\mu_d$ , that falls within a Hele-Shaw cell filled with a fluid of density  $\rho_a$  and molecular viscosity  $\mu_a$ . The two fluids are miscible, hence there is no surface tension between them. In addition, we consider that the diffusivity between the two fluid is low enough so that no significant mixing takes place between them. The viscosity ratio is defined as  $\lambda \equiv \mu_a/\mu_d$ , and the elongation ratio as  $\alpha \equiv b/a$ . We denote by  $R$  the characteristic radius of the drop, i.e., the radius of a circular disk with the same area as the drop. The distance between the two plates of the cell, i.e., the gap width, is denoted  $H$ . The thickness of the drop within the gap (i.e., orthogonally to the plane of the cell) is denoted by  $w(x, z, t)$ . We denote by  $w_*(t)$  the characteristic thickness of the drop. This is taken as the spatial average of  $w(x, z, t)$  over an area excluding the interface around the circumference of the drop [see Fig. 1(b)]. In the following, we obtain analytically an expression of the falling velocity of an elliptical drop whose thickness  $w_*$  is smaller than the gap width of the cell:  $w_* < H$ .

As discussed in the introduction, several studies [6,16,17,33] came up with predictions of the falling velocity of a drop or a bubble in a Hele-Shaw cell, in the case where the drops span the entire gap of the cell ( $w_* = H$ ). They predicted that the falling velocity of the drop did not depend on the radius  $R$  and scaled with

$$U = U_0 \equiv \frac{H^2 \Delta \rho g}{12 \mu_a}, \quad (1)$$

where  $\Delta\rho = \rho_d - \rho_a$ . Maxworthy [6] studied the influence of the aspect ratio of elliptical bubbles and determined that the bubble velocity is equal to  $\alpha U_0$ . Bush [16] and Gallaire *et al.* [17] investigated the case of drops of non-negligible viscosity, and came up with an expression of the drop velocity. In the absence of Marangoni effects and at the leading order they found the scaling velocity to scale with

$$U = U_0 \frac{\lambda}{\lambda + 1}. \quad (2)$$

In the limit of  $\lambda \gg 1$  ( $\mu_a \gg \mu_d$ ), this matches the prediction (1) for circular drops. Keiser *et al.* [11] conducted a study of drops that were much more viscous than the ambient fluid ( $\lambda \ll 1$ ), having a thin lubrication film between the drop and the walls of the cell ( $w_* \lesssim H$ ). They proposed an analytical expression of the falling velocity of a drop [Eq. (3.8) of [11]]:  $U = U_0[3(1 - w_*/H) + \lambda]$ . For  $\lambda \ll 1$ , they found that the only non-negligible source of energy dissipation was the friction between the flat sides of the drop and the lubrication film. Therefore, they neglected all other sources of energy dissipation, in particular that resulting from the flow in the bulk of the ambient fluid. In the following, we propose a theory predicting the falling velocity of elliptical drops with a lubrication film of any thickness ( $w_* < H$ ) and for all  $\lambda$ .

We consider an elliptical drop of half-width  $a$  and half-height  $b$  [see Fig. 1(a)], translating at a constant velocity  $\mathbf{U} = U\mathbf{e}_z$  in the  $z$ -direction. The acceleration of gravity  $\mathbf{g} = g\mathbf{e}_z$  is directed along the  $z$ -axis. We set ourselves in a frame moving with the drop. In this frame, the walls of the cell are moving upwards at a constant velocity of  $-U\mathbf{e}_z$ . We denote by  $\mathbf{u}_a(x, y, z)$  the velocity of the ambient fluid, and by  $\mathbf{u}_d(x, y, z)$  that in the drop. The drop thickness  $w_*$  and elongation ratio  $\alpha$  are determined empirically. At low Reynolds number, the equations governing the flow in the Hele-Shaw cell are the 3D Stokes equations for an incompressible fluid:

$$\mu_a \frac{\partial^2 \mathbf{u}_a}{\partial y^2} = -\nabla P_a, \quad (3)$$

in the ambient fluid, and

$$\mu_d \frac{\partial^2 \mathbf{u}_d}{\partial y^2} = -\nabla P_d - \Delta\rho\mathbf{g}, \quad (4)$$

in the drop, where  $P_a$  and  $P_d$  denote the pressure in the ambient fluid and in the drop, respectively, and  $\Delta\rho = \rho_d - \rho_a$ .

We solve Eqs. (3) and (4) in two different regions: far from the drop [region 1 in Fig. 1(c)], and between the drop and the walls of the cell [region 2 in Fig. 1(c)]. Far from the drop, Eq. (3) gives, using boundary conditions  $\mathbf{u}_a(y \pm H/2) = -U\mathbf{e}_z$ :

$$\mathbf{u}_{a,1} = \frac{\nabla P_a}{2\mu_a} \left[ \left( \frac{H}{2} \right)^2 - y^2 \right] - \mathbf{U}. \quad (5)$$

between the drop and the walls [region 2 in Fig. 1(c)], we solve Eqs. (3) and (4) using no-slip boundary conditions at  $y=H/2$ , continuity of velocity and tangential stress at  $y=w_*/2$  and symmetry of the flow across the  $y=0$  plane (hence  $\partial u_d/\partial y|_{y=0} = 0$ ). This gives

$$\begin{aligned} \mathbf{u}_d = & \frac{\nabla P_d}{2\mu_d} \left\{ \frac{1}{\lambda} \left[ \left( \frac{H}{2} \right)^2 - \left( \frac{w_*}{2} \right)^2 \right] + \left[ \left( \frac{w_*}{2} \right)^2 - y^2 \right] \right\} \\ & + \frac{\Delta\rho g z}{2\mu_d} \left\{ \frac{w_*}{\lambda} \left( \frac{H}{2} - \frac{w_*}{2} \right) + \left[ \left( \frac{w_*}{2} \right)^2 - y^2 \right] \right\} - \mathbf{U}. \end{aligned}$$

We define the  $y$ -averaged velocity fields,  $\tilde{u}_a(x, z)$  and  $\tilde{u}_d(x, z)$ , as the average of  $\mathbf{u}_a$  and  $\mathbf{u}_d$  over the thickness of the ambient and drop fluid, respectively:

$$\tilde{u}_a(x, z) = \frac{1}{H} \int_{-H/2}^{H/2} \mathbf{u}_{a,1}(x, y, z) dy = -\frac{\nabla P_a}{12\mu_a} H^2 - \mathbf{U}, \quad (6)$$

$$\tilde{u}_d(x, z) = \frac{1}{w_*} \int_{-w_*/2}^{w_*/2} \mathbf{u}_d(x, y, z) dy = -\frac{\nabla P_d}{12\mu_d} w_*^2 \beta - \frac{\Delta\rho\mathbf{g}}{12\mu_d} w_*^2 \gamma - \mathbf{U}, \quad (7)$$

with  $\beta = 1 + \frac{3}{2} \frac{1}{\lambda} [(\frac{H}{w_*})^2 - 1]$  and  $\gamma = 1 + \frac{3}{\lambda} (\frac{H}{w_*} - 1)$ .

In the  $(x, z)$  plane, the flow is inviscid, irrotational, and incompressible. We can therefore use potential theory to describe the flow in the plane of the cell [5]. Defining velocity potentials  $\nabla\phi_a = \tilde{u}_a$  and  $\nabla\phi_d = \tilde{u}_d$ , we can express the pressure as a function of the velocity potential using (6) and (7):

$$P_a = \frac{12\mu_a}{H^2} (-\phi_a + Uz), \quad (8)$$

$$P_d = -\frac{12\mu_d}{w_*^2} \frac{1}{\beta} \phi_d - \frac{\gamma}{\beta} \Delta\rho gz + \frac{12\mu_d}{w_*^2} \frac{1}{\beta} Uz. \quad (9)$$

We obtain the expression of the velocity potential of the flow around an ellipse by using a Joukowski transformation [34] and the well-known expression of the velocity potential of the flow around a disk. This calculation is done in the Appendix and yields, at the interface,

$$\phi_a|_{\partial D} = U \left( z + \frac{1}{\alpha} z \right), \quad (10)$$

where  $\alpha \equiv b/a$  is the aspect ratio of the drop.

Requiring continuity of pressure at the interface, we must have  $\phi_d = 0$  within the drop. The velocity  $U$  of the drop is thus found to be

$$U = \alpha \frac{\Delta\rho g H^2}{12\mu_a} \frac{1 + 3\frac{1}{\lambda} (\frac{H}{w_*} - 1)}{1 + \frac{1}{\lambda} \left[ \frac{H^2}{w_*^2} (\alpha + \frac{3}{2}) - \frac{3}{2} \right]}. \quad (11)$$

This expression matches the analytic expression (2) obtained by [16,17] for the case of a circular drop ( $\alpha = 1$ ) whose thickness is equal to the span of the cell. It also matches that of Keiser *et al.* [11] for circular drops with  $\lambda \ll 1$  and  $w_* \sim H$ .

### III. EXPERIMENT SETUP AND ANALYSIS METHODS

#### A. Drop and ambient fluids

We injected drops made of a solution of glucose syrup and water into an ambient fluid made of a solution of UCON oil and water. Both glucose syrup and UCON oil are fully miscible in water. Across all experiments, the density,  $\rho_d$ , of the drop was larger than that of the ambient fluid  $\rho_a$ , while its viscosity,  $\mu_d$ , was lower than that of the ambient fluid  $\mu_a$ . The density and viscosity of the two fluids were adjusted by varying the concentrations of glucose syrup and UCON oil. A few drops of food dye were mixed with the drop fluid to enhance their contrast with the ambient fluid and make possible measurements of the drop thickness using light attenuation. Densities of the dyed solutions were measured using an Anton Paar DMA35 densitometer, and viscosities were measured with a Kinexus Malvern rheometer. Measured values are plotted in Fig. 2(a). The room temperature was measured for each experiment, and the viscosity was corrected accordingly. The influence of temperature on the density of the fluids was, however, found to be negligible. With these fluids, the viscosity ratio  $\lambda = \mu_a/\mu_d$  varied between 5.50 and 270, and the density difference  $\Delta\rho = \rho_d - \rho_a$  varied between  $3.8 \text{ kg m}^{-3}$  and  $222 \text{ kg m}^{-3}$ . In turn, the dimensionless density difference  $\Delta\rho/\rho_a$  varied between  $3.5 \times 10^{-3}$  and 0.21 [Fig. 2(b)].

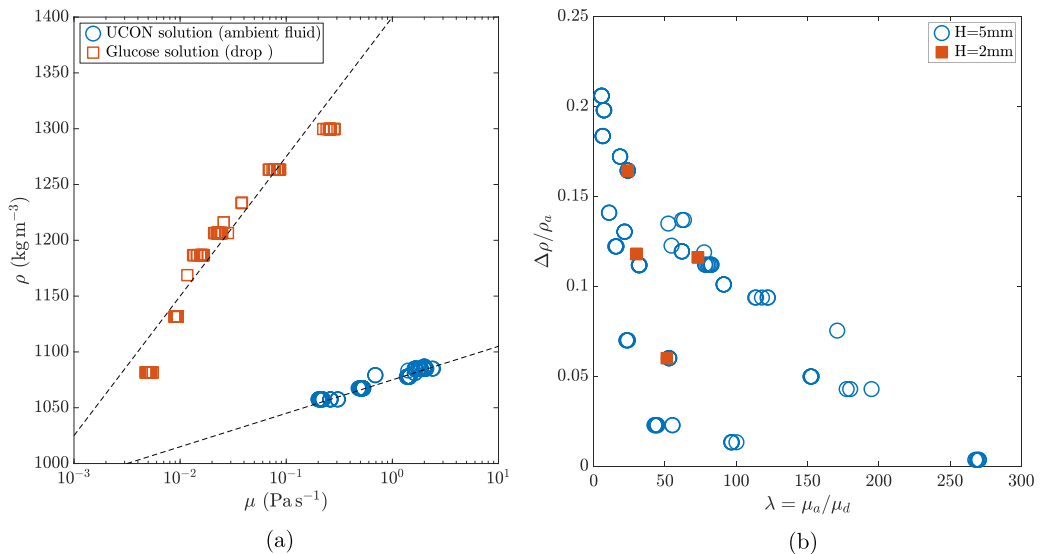


FIG. 2. (a) Plot of the density of the ambient and drop fluid vs their viscosity. The black dashed lines correspond to fits  $\rho_a = 1075 + 30 \log_{10} \mu_a$  and  $\rho_d = 14000 + 125 \log_{10} \mu_d$ . (b) Parameters  $\lambda$  and  $\Delta\rho/\rho_a$  of all the experiments performed. The symbols indicate the width of the gap.

### B. Experimental cell and optical measurements

We study the fall of drops into a more viscous ambient fluid, in a laterally confined vertical Hele-Shaw cell. The cell was  $20 \text{ cm} \times 30 \text{ cm}$ , with a gap of  $H = 5 \text{ mm}$ . To check the influence of  $H$ , some experiments were also conducted in a cell with a gap of  $H = 2 \text{ mm}$ . Fewer experiments were done with  $H = 2 \text{ mm}$  because it was challenging to create drops of the same radius as with  $H = 5 \text{ mm}$  without the drop becoming unstable. In total, 118 experiments were run with  $H = 5 \text{ mm}$ , and 6 with  $H = 2 \text{ mm}$ . Analyses presented here are with  $H = 5 \text{ mm}$  unless specified otherwise. The drops were injected into the cell from the top using a syringe. The injection time of the drops was kept short (on the order of 1 second), so that the injection was complete before the drop fell significantly. We also wished to keep the drop size approximately the same across our experiments. Hence special care was taken to inject the same volume of fluid each time. In all experiments, the drop radius was larger than the gap width and much larger than the drop thickness. The average drop radius was  $1.05 \pm 0.06 \text{ cm}$  for experiments with  $H = 5 \text{ mm}$  and  $0.91 \pm 0.15 \text{ cm}$  for experiments with  $H = 2 \text{ mm}$ . No mixing was observed between the drop and ambient fluid across all of our experiments.

An LED panel was placed behind the cell, and a sCMOS PCO Edge 4.2 camera with a Nikon Nikkor 24 mm f/2.8 lens recorded images of the fall of the plume from the front of the cell. An example of a raw camera image, cropped around the drop, is shown in Fig. 3(a). As will be discussed in more detail later, the drops exhibited a tear-drop shape and left behind them a thin tail.

An image-processing algorithm was used to separate pixels belonging to the moving drop from those belonging to the tail using morphological operations. The successive snapshots were first converted to binary, black and white images. Then they were morphologically opened using the MATLAB function `imopen`, with a morphological element whose size (15 pixels) was slightly bigger than the span of the tail (about eight pixels for all experiments), hence “erasing” the tail from the image. The remaining pixels were attributed to the drop. An example of the output of the image processing algorithm can be seen as the superimposed red contour in Fig. 3(a). Because the span of the tail was nearly constant for all cases (approximately 1 mm), this method simply and efficiently separated pixels belonging to the drop from those belonging to the tail. Once the drop

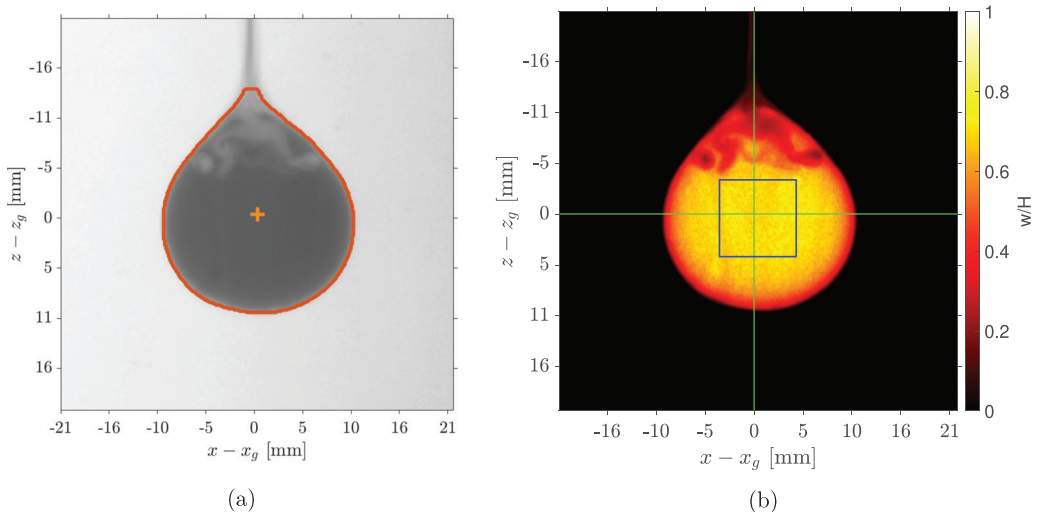


FIG. 3. (a) Raw image and (b) measurement of fluid thickness  $w/H$  of a drop of  $(\mu_d, \rho_d) = (1.57 \times 10^{-2} \text{ Pas}^{-1}, 1186 \text{ kgm}^{-3})$  falling in an ambient fluid of  $(\mu_a, \rho_a) = (1.44 \text{ Pas}^{-1}, 1078 \text{ kgm}^{-3})$ . On (c) the contour (red line) and centroid (red cross) of the detected plume are highlighted. On (d), the colormap shows measurements of  $w/H$ , the green cross highlights where the profiles of Fig. 5(a) are measured on the drop, and the blue square shows where the average of the fluid thickness,  $w_*$ , is computed (see Sec. IV A).

pixels were known, we computed the position  $(x_g, z_g)$  of its center of gravity, its half-width  $a$ , its half-height  $b$ , and its elongation ratio  $\alpha = b/a$ . We also computed its equivalent radius  $R$ .

The vertical velocity of the drop  $v_z$  was computed as the average of its instantaneous vertical velocity over a time span that avoided the initial transient effects from the injection and the late-time break-up of the drop, if this occurred. Drops traveled on average over 12 drop radii for cases with no break-up, and seven for cases with break-up. The elongation ratio was not constant in time for a given drop, but varied by about 10% in experiments with  $H=5$  mm. As done for  $v_z$ , we computed an average value of the elongation ratio and of the drop thickness.

In addition to measuring the position of the drop in the plane of the cell, we also measured the thickness of the drop  $w$ , as shown in Fig. 1(b). This was done by measuring the attenuation of light that was absorbed by dye when passing through the plume. Pioneered by Obaton and Tritton [35], and subsequently used by Lajeunesse *et al.* [22] to measure the thickness of fluid displacement in a Hele-Shaw cell, measuring light absorption offers a nonintrusive way of determining the thickness of thin liquid films. According to the Beer-Lambert law, the light intensity  $I$  that passes through a drop where its thickness is  $w$  is

$$I = I_\infty + (I_0 - I_\infty)e^{-w/\sigma_h}, \quad (12)$$

where  $I_\infty$  is the effective “black” light intensity,  $I_0$  is the background light intensity, measured in the absence of drop fluid in the cell, and  $\sigma_h$  is the e-folding distance over which the intensity difference decreases by a factor  $e$ . The background light intensity  $I_0$  is obtained for each experiment by measuring the light intensity before the release of a drop.  $I_\infty$  and  $\sigma_h$  are determined using a wedge-shaped calibration cell in which there was a linear variation of the thickness of fluid. The calibration tank was filled with the fluid used to make the drops. This gave a measure of  $I(w)$  for a linear variation of  $w$ . We then fit  $I(w)$  to the exponential curve given by (12), thus determining the remaining empirical parameters  $I_\infty$  and  $\sigma_h$ . With the resulting calibration curve, it was straightforward to deduce the drop thickness  $w$  from measurements of  $I$ .



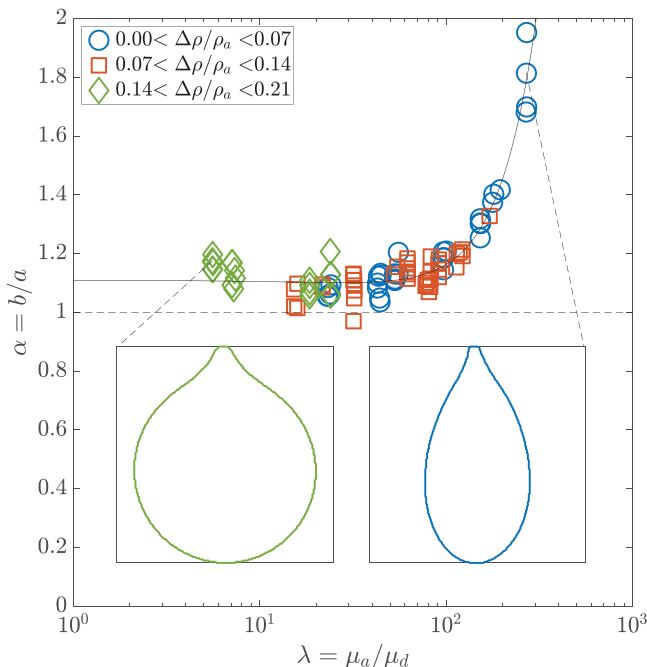


FIG. 4. Plot of the plume elongation ratio  $\alpha$  vs the viscosity ratio  $\lambda$ . Symbols discriminate between different values of  $\Delta\rho/\rho_a$ . The black curve shows the quadratic fit  $\alpha = 1.17 \times 10^{-5}\lambda^2 - 6.40 \times 10^{-4}\lambda + 1.11$ . The insets show the shape of drop for experiments on the left with  $(\mu_a, \mu_d) = (1.10, 3.43 \times 10^{-1}) \text{ Pas}^{-1}$ ,  $\Delta\rho/\rho_a = 2.12 \times 10^{-1}$  and on the right with  $(\mu_a, \mu_d) = (1.10, 2.40 \times 10^{-3}) \text{ Pas}^{-1}$ ,  $\Delta\rho/\rho_a = 5.50 \times 10^{-3}$ .

#### IV. DROP SHAPE, FALL VELOCITY, AND STABILITY

In the following section, we present experimental measurements of the drop shape and thickness, and of the thickness of the tail left behind the drop. We then present measurements of the drop falling velocity, and compare them with our theoretical expression. Finally, we present data on the stability of the drop and document the break-up phenomenon.

##### A. Shape and thickness

In our experiments, the drops became slightly elongated in shape as they descended. Figure 4 plots the measured aspect ratio,  $\alpha$ , of the drops versus the viscosity ratio  $\lambda = \mu_a/\mu_d$  of the ambient to drop molecular viscosity. Across all of our experiments, we found an average elongation ratio of  $1.2 \pm 0.06$ , with most drops being close to a circular disk shape for  $\lambda \lesssim 100$ . As the viscosity ratio increased, so did  $\alpha$ , being as large as 1.8 for  $\lambda = 270$ . From experiments with  $H=5$  mm, we found an empirical quadratic fit for the relationship between the aspect ratio and the viscosity ratio of the drops:

$$\alpha = 1.17 \times 10^{-5}\lambda^2 - 6.40 \times 10^{-4}\lambda + 1.11. \quad (13)$$

We do not present the elongation ratio for drops with  $H=2$  mm because the shape of the drop varied significantly as it fell.

Using the light absorption technique described, we measured the drop thickness  $w(x, z, t)$ , as illustrated in Fig. 3(b). The viscosity ratio,  $\lambda$ , did not have a significant impact on the value of  $w/H$  in our space of parameters. Figure 5(a) shows two different profiles of  $w/H$  taken along horizontal and vertical cross sections as indicated by the two blue lines shown in Fig. 3(b). In the horizontal direction ( $x$ ), the drop thickness is nearly constant in the bulk of the drop, then decreases sharply at



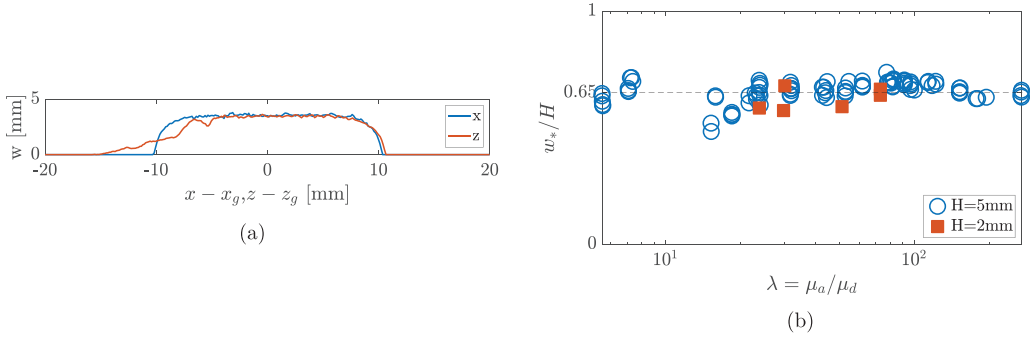


FIG. 5. (a) Profiles of drop thickness versus the position  $x$  or  $z$  centered on the centroid of the drop. This is the same drop as that shown in Fig. 3(b) [ $(\mu_d, \rho_d) = (1.57 \times 10^{-2} \text{ Pas}^{-1}, 1186 \text{ kgm}^{-3})$ ,  $(\mu_a, \rho_a) = (1.44 \text{ Pas}^{-1}, 1078 \text{ kgm}^{-3})$ ], and the profiles are taken along the blue lines. (b) Plot of the average drop thickness over gap width  $w_*/H$  for different values of  $H$ .

the interface. In the vertical direction, the same behavior is observed, except that the drop thickness tapers down near its tail. In both cases the thickness profiles form a plateau in the bulk of the drop. We measured the characteristic thickness  $w_*$  as a spatial average over this plateau region. In order to do this, we averaged the values of  $w(x, z, t)$  in an area [shown by a blue rectangle in Fig. 3(b)], chosen to avoid the drop boundaries. This spatial average was averaged in time over the same time span as  $v_z$  and  $\alpha$ ,  $w_* = \bar{w}(x, z, t)$ . For all fluid combinations, and for  $H=5$  mm or 2 mm, we found a constant ratio  $w_*/H$  of about  $0.65 \pm 0.03$ . Figure 3(b) also shows a distinctive feature of our experiments, namely, the presence near the tail of the drop of a triangular-shaped area containing blobs where light attenuation was reduced. These blobs, which are thought to be inclusions of ambient fluid within the drop, conveniently revealed motion occurring within the drop due to nonuniformity in composition and/or thickness.

Our measurements of the drop thickness can be compared with previous work. Shukla *et al.* [13] performed experimental measurements of the thickness of highly confined ( $R/H \in [1, 2]$ ), immiscible drops with  $\lambda \in [1, 11]$  falling into a more viscous fluid in a Hele-Shaw cell with  $H$  between 4.59 mm and 4.80 mm. Their values of  $w_*/H$  ranged from 0.72 to 0.90, decreasing with decreasing capillary number (Ca going from  $3 \times 10^{-2}$  to 0.35 in which Ca measures viscous drag relative to surface tension) and decreasing  $\lambda$ . Experiments and numerical simulations with pressure-driven immiscible drops in microfluidic channels [9,12,15] showed that  $w_*/H$  was close to unity for  $\lambda < 1$ . This stands in contrast to previous experimental results for miscible displacements spanning the entire width of the Hele-Shaw cell [22,23,36,37], which found a constant value of  $w_*/H \sim 0.50$  for  $1 < \lambda < 1000$  and negligible diffusivity between the two fluids. Petitjeans *et al.* [23] predicted that the ratio of the thickness of a miscible displacement in a Hele-Shaw cell to that of the gap of the cell reached a value of  $2/3$  if the flow in the cell was representative of a Poiseuille flow across the entire width of the cell. Our experimental results are very close to this value.

In our experiments a thin tail of fluid extends behind the drop. A similar structure was observed, but not discussed by Garcimartín *et al.* [7] in their study of drops in a Hele-Shaw cell with  $R \sim H$ . For all of our experiments, the width of the tail  $a_{\text{tail}}$  [in the direction  $x$ ; see Fig. 1(a)] was constant with  $a_{\text{tail}} \simeq 1$  mm, while the tail thickness  $w_{\text{tail}}$  [in the direction  $y$ ; see Fig. 1(b)] ranged from 0.3 mm to 1 mm with a slight dependence on  $\lambda$ . In turn, the ratio  $w_{\text{tail}}/H$  varied between 0.05 and 0.2. We present measurements of  $a_{\text{tail}}$  scaled by the width of the drop  $a$  and of the tail aspect ratio  $a_{\text{tail}}/w_{\text{tail}}$ , respectively, in Fig. 6.

We investigated whether this tail was created by residual fluid resulting from the injection that then sinks in the wake of the drop, or whether the tail of fluid was released by the drop during its fall. In a 3D medium with miscible drops, Shimokawa *et al.* [28] and Shimokawa and Sakaguchi [32] observed a tail behind the drop, which seemed to be linked to the injection, because the drop

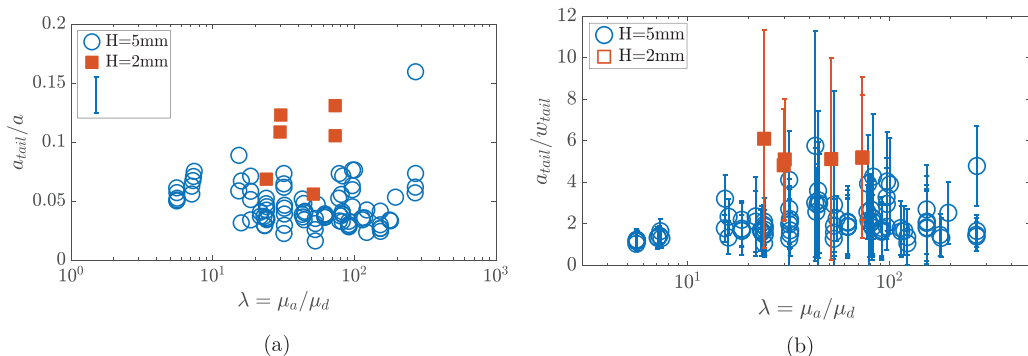


FIG. 6. Plot of the tail (a) width (in the  $x$  direction) scaled by the width of the drop, with a typical error bar showing error linked to a detection error of about one pixel from each side of the tail in the legend box (b) aspect ratio vs the viscosity ratio  $\lambda$ , for  $H=5$  mm (open symbols) and  $H=2$  mm (filled symbols).

eventually detached from the tail. In our experiments, however, measurements of drop thickness revealed that the volume of the drop shrank continuously as the drop fell. The total volume of fluid in the cell (i.e., the sum of the drop and tail volume) remained nearly constant (variations of less than 10% were observed, as seen in Fig. 7), this suggests that there is no flux of fluid coming from the injection site, the tail results from fluid being extracted from the drop during its fall.

### B. Fall velocity

The velocity of the drop ranged between  $0.5 \text{ mms}^{-1}$  and  $11 \text{ mms}^{-1}$  across our experiments with  $H=5$  mm, and between  $0.3 \text{ mms}^{-1}$  and  $1.1 \text{ mms}^{-1}$  for our experiments with  $H=2$  mm. Using the thickness of the gap  $H$  as a characteristic length, and the measured mean drop velocity  $v_z$  as a characteristic velocity, the Reynolds number  $\text{Re} = v_z H / \nu_a$ , ranged between  $2.4 \times 10^{-3}$  and  $3.4 \times 10^{-1}$  for our experiments in  $H=5$  mm, and between  $4.7 \times 10^{-4}$  and  $5.6 \times 10^{-3}$  for our experiments in  $H=2$  mm.

Figure 8(a) shows the drop velocity plotted versus the viscosity ratio  $\lambda$ . The drop velocity shows no clear trend with  $\lambda$ . Figure 8(b) shows the drop velocity plotted versus the predicted velocity

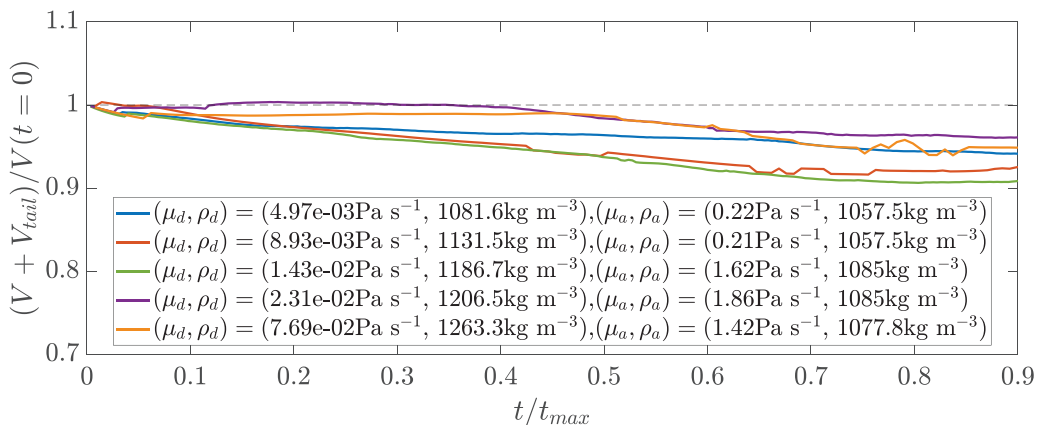


FIG. 7. Plot of the variation of the total volume of drop fluid in the cell, scaled by that of the drop at  $t = 0$ ,  $(V + V_{\text{tail}})/V(t = 0)$ , as a function of the time scaled by the total falling time,  $t_{\text{max}}$ ,  $t/t_{\text{max}}$  for 10 different drops. The measurement error on the volume of the drop is of about 10%.

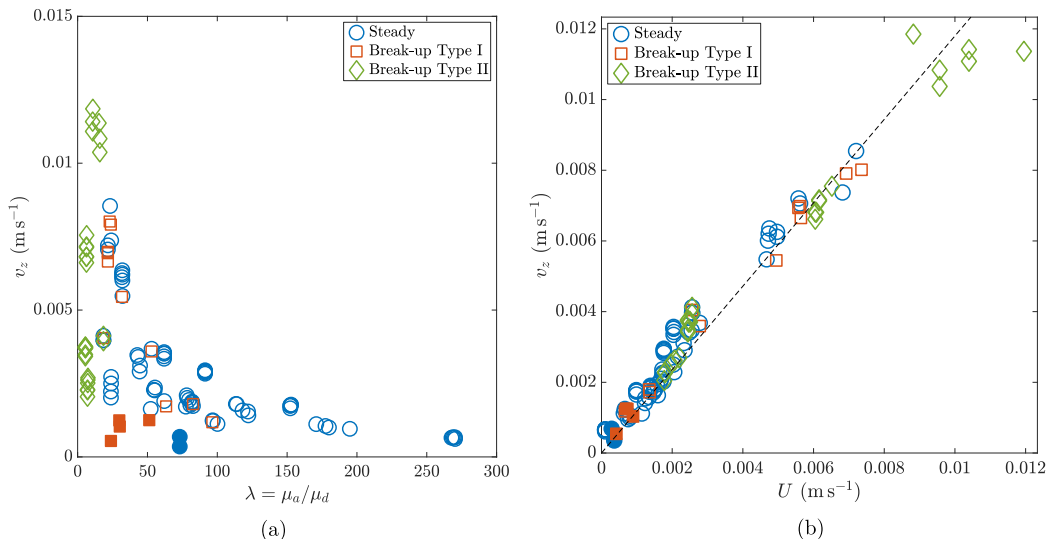


FIG. 8. Plot of the drop falling velocity  $v_z$  versus (a) the viscosity ratio,  $\lambda$  (b)  $U$ , given by (11). The mean drop equivalent radius is  $R = 1.05 \pm 0.1$  cm for  $H = 5$  mm (open symbols), and  $R = 0.91 \pm 0.3$  cm for  $H = 2$  mm (filled symbols). The symbols discriminate the points based on their behavior. The black dashed curve shows  $v_z = 1.18U$ .

$U$  given by (11). In our expression of  $U$ , we calculate  $\alpha$  using the quadratic fit (13), for points with  $H=5$  mm. For points with  $H=2$  mm we used the measured value of  $\alpha$ , despite poor accuracy because of the instability of the shape of the drop. For both values of  $H$ , we take  $w_*/H = 0.65$ . Although the theory collapses the data onto a line, the slope is not equal to unity. Instead, a linear best fit gives  $v_z = CU$  with  $C = 1.18 \pm 0.03$ . The fact that  $C$  is not equal to 1 is likely a consequence of the drop thickness  $w(x, z, t)$  not being uniform across the entire drop [see Fig. 3(b)], as assumed in the theory. In particular, the drop thickness decreases significantly near the tail, and the drops have a teardrop, not elliptical, shape. Nonetheless, Fig. 8 shows a good collapse of the experimental data with the theory after being adjusted by an empirical coefficient.

### C. Drop stability

Within the space of parameters studied [see Fig. 2(b)], drops are seen to adopt three main types of stability behavior as they depend upon the relative viscosities and densities of the drop and ambient fluids. The first is a quasisteady, stable drop, during which there is no significant horizontal deviation of its trajectory or shape. The second features a break up of the drop due to instability of the drop itself, which we refer to as Type I break-up. The third features a break up of the drop, triggered by inclusions of ambient fluid, which we refer to as Type II break-up.

Snapshots of the fluid thickness for a quasisteady, stable drop are shown in Fig. 9(a). The corresponding movies can be seen as Supplemental materials [38]. Near the tail of the drop there are dark spots associated with inclusions of ambient fluid within the drop. Such inclusions were observed for all the drops in our experiments. Although the shape of the drop oscillates during its descent, no break-up of the drop occurred.

In the case of a Type I break-up, the interface near the bottom of the drop spontaneously flattened and formed into a concave shape [Fig. 9(b)]. The drop then split and formed two daughter drops. In some experiments, the flattening was sufficiently close to the bottom of the drop, that the break-up generated two daughter drops of comparable size. In experiments where the flattening developed to

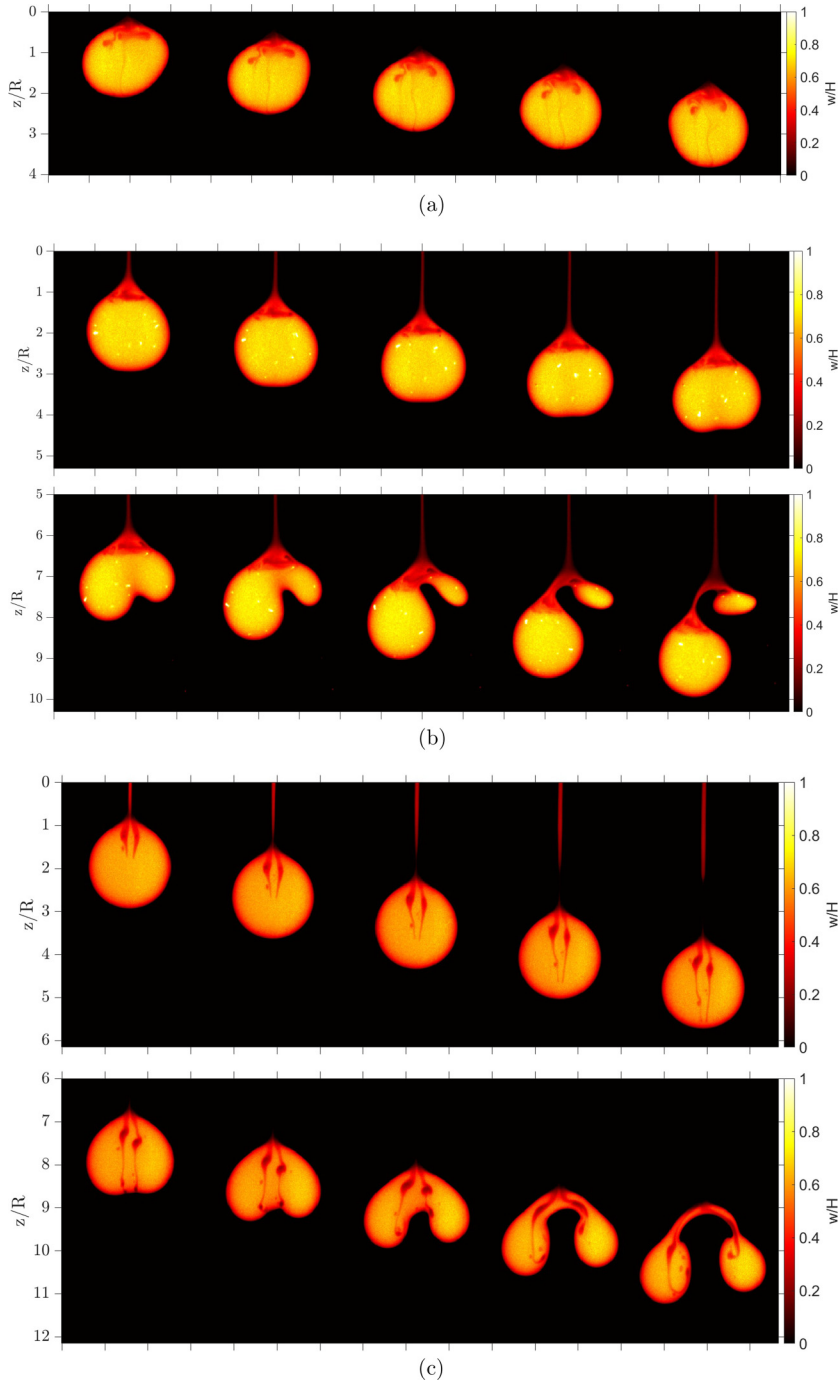


FIG. 9. Successive snapshots of drops with (a)  $\mu_d = 1.66 \times 10^{-2} \text{ Pas}^{-1}$ ,  $\Delta\rho/\rho_a = 0.11$ , (b)  $\mu_d = 5.20 \times 10^{-3} \text{ Pas}^{-1}$ ,  $\Delta\rho/\rho_a = 1.33 \times 10^{-2}$ , (c)  $\mu_d = 2.53 \times 10^{-1} \text{ Pas}^{-1}$ ,  $\Delta\rho/\rho_a = 0.21$ .  $\mu_a = 0.53 \text{ Pas}^{-1}$  for (a),  $\mu_a = 0.51 \text{ Pas}^{-1}$  for (b), and  $1.41 \text{ Pas}^{-1}$  for (c). The break-up type is Type I for (b) and Type II for (c). The time interval between two snapshots is 0.8 s for (a), 5.0 s for (b), and 2.5 s for (c). The drop radius  $R$  is 1.04 cm for (a), 0.99 cm for (b), and 1.07 cm for (c). The colormap shows  $w/H$ . The vertical and horizontal scales are identical.

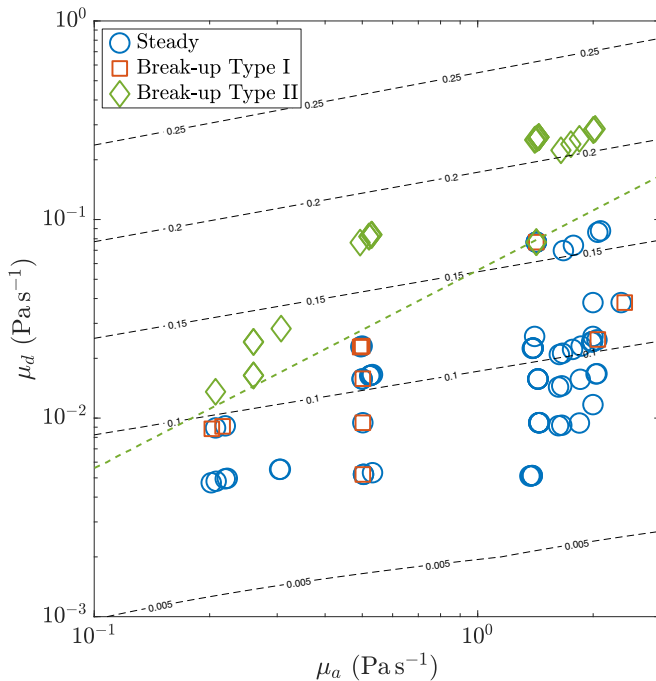


FIG. 10. Map of the experiments performed on the space of parameters  $(\mu_a, \mu_d)$ . The isocontours show values of  $\Delta\rho/\rho_a$ . Symbols show the type of behavior observed. The green dashed line shows the separation between  $\lambda < 18$  (above the line) and  $\lambda > 18$  (below the line).

one side of the drop [as in Fig. 9(b)], one of the daughter drops was significantly smaller than the other. This smaller drop was then caught in the wake of the larger drop and merged back with it.

In the case of Type II break-up, spotlike defects near the tail of the drop move downward toward the bottom interface of the drop [Fig. 9(c)]. When they came into contact with the interface, they triggered the break-up. Their motion is thought to be caused by internal fluid motion within the drop.

Figure 10 distinguishes these three behaviors as they depend on the viscosity of the drop and ambient fluid. Type II break-up was only observed in experiments with  $\lambda \lesssim 18$ . The fact that the viscosity of the ambient and drop fluids are close for Type II break-ups is thought to facilitate the presence of inclusions of ambient fluid within the drop, in turn leading to break-up through vertical advection of the inclusions. For  $\lambda \gtrsim 18$ , both stable drops, and drops undergoing Type I break-up are observed, sometimes with the same experimental parameters. This suggests that Type I break-ups are caused by an instability of the shape of the drop, arising from small-scale perturbations associated with the injection process.

## V. DISCUSSION AND CONCLUSION

We presented experimental measurements of the shape, thickness and velocity of miscible viscous drops falling in a Hele-Shaw cell for a large range of viscosity ratios ( $5.5 < \lambda < 270$ ) and corresponding density ratios ( $3.5 \times 10^{-3} < \Delta\rho/\rho_a < 0.21$ ).

Our experiments showed that miscible drops could be significantly elongated, and were approximately half the thickness of the gap of the cell ( $w_*/H \sim 0.65 \pm 0.03$ ). We also showed that miscible drops could break-up in a fashion closely resembling that of immiscible drops [19]. We extended existing predictions for the falling velocity of near-circular drops with thickness close to or equal

to the thickness of the gap of the cell  $H$  [16,17] to account for drop thickness smaller than the gap, elongation and viscosity ratios  $5 < \lambda < 270$ . Our theory is supported by a good prediction of the falling velocity. It collapses data for a wide range of parameters, regardless of the break-up of the drops, although the observed speed is larger by an empirical constant of about 1.18.

Despite experimental observation of internal fluid motion in the drop, our theory predicts that at the leading order, all the fluid inside the drop moves at the same velocity (i.e. the velocity of the drop). The motion of fluid within the drop must therefore be an effect of higher order. This is evident by the fact that neither the break-up of drops, nor the presence of internal fluid motion had an impact on the falling velocity of the drops. Although no calculation of the magnitude of internal fluid motion within the drop was undertaken, we found that fluid motion within the drop could cause the break-up of the drop, when the viscosity ratio is low enough ( $\lambda < 18$ ; Type II break-up). In this case, we believe that the break-up time of the drop can be determined from the magnitude of the downward flow within the drop and the buoyancy of the inclusion of ambient fluid. Type I break-ups (with  $\lambda > 18$ ) are likely caused by an instability of the shape of the drop resulting from small perturbations upon injection. We observed several drops that underwent oscillations without breaking up. It is possible that these drops would eventually undergo a Type I break-up that could not be observed before they exited the observation area. Our findings on the dynamics of confined miscible drops may prove insightful for several applications where immiscible droplets are normally used.

#### ACKNOWLEDGMENTS

We thank M. Moulin for the design of the experimental setup. This work was supported by the LABEX iMUST (Grant No. ANR-10-LABX-0064) of Université de Lyon, within the program “Investissements d’Avenir” (Grant No. ANR-11-IDEX-0007) operated by the French National Research Agency (ANR).

#### APPENDIX: TRANSFORMATION FROM THE FLOW AROUND A DISK TO THAT AROUND AN ELLIPSE

The velocity potential of the flow around a circular cylinder in a uniform flow is well known. We can use a Joukowski transformation [34], to transform this velocity potential into that around an elliptical cylinder. Let us consider a disk  $\zeta_1$  of radius  $R = (a + b)/2$  in the  $(x_1, z_1)$  plane, and an ellipse  $\zeta_2$  of semiminor axis  $a$  and semimajor axis  $b$  in the  $(x_2, z_2)$  plane, so that  $\zeta_1 = x_1 + iz_1$  and  $\zeta_2 = x_2 + iz_2$ . The complex potential of the flow around the circle  $\zeta_1$  in a uniform flow of far-field velocity  $\mathbf{U} = U\mathbf{e}_z$  is

$$\Phi = U \left( \zeta_1 + \frac{R^2}{\zeta_1} \right). \quad (\text{A1})$$

The Joukowski transformation,

$$\zeta_2 = \zeta_1 + \left( \frac{a - b}{4} \right)^2 \frac{1}{\zeta_1}, \quad (\text{A2})$$

transforms the circle  $\zeta_1$  onto the ellipse  $\zeta_2$ .

In order to get the expression of the velocity potential around the ellipse  $\zeta_2$ , we solve the quadratic equation (A2), taking the positive solution because it is the only relevant one:

$$\zeta_1 = \frac{\zeta_2 + [\zeta_2^2 + (a^2 - b^2)]^{1/2}}{2}. \quad (\text{A3})$$

Substituting (A3) into (A1) gives the complex potential

$$\Phi = \frac{U}{a - b} \left\{ -b\zeta_2 + a[\zeta_2^2 + (a^2 - b^2)]^{1/2} \right\}. \quad (\text{A4})$$

The velocity potential is obtained by taking the real part of the complex potential:  $\phi = \Re\Phi$ . Evaluating  $\phi$  on the boundary of the ellipse gives

$$\phi = Uz_1 \left( 1 + \frac{a}{b} \right). \quad (\text{A5})$$

- 
- [1] R. Farajzadeh, A. Andrianov, and P. L. J. Zitha, Investigation of immiscible and miscible foam for enhancing oil recovery, *Ind. Eng. Chem. Res.* **49**, 1910 (2010).
- [2] P. Calvert, Inkjet printing for materials and devices, *Chem. Mater.* **13**, 3299 (2001).
- [3] S.-Y. Teh, R. Lin, L.-H. Hung, and A. P. Lee, Droplet microfluidics, *Lab Chip* **8**, 198 (2008).
- [4] A. Haugen, N. Mani, S. Svenningsen, B. Brattekkås, A. Graue, G. Ersland, and M. A. Fernø, Miscible and immiscible foam injection for mobility control and {EOR} in fractured oil-wet carbonate rocks, *Transp. Porous Media* **104**, 109 (2014).
- [5] P. G. Saffman and G. Taylor, The penetration of a fluid into a porous medium or Hele-Shaw cell containing a more viscous liquid, *Proc. Math. Phys. Eng. Sci.* **245**, 312 (1958).
- [6] T. Maxworthy, Bubble formation, motion and interaction in a Hele-Shaw cell, *J. Fluid Mech.* **173**, 95 (1986).
- [7] A. Garcimartín, H. L. Mancini, and C. Pérez-García, 2D Dynamics of a drop falling in a miscible fluid, *Europhys. Lett.* **19**, 171 (1992).
- [8] A. Eri and K. Okumura, Viscous drag friction acting on a fluid drop confined in between two plates, *Soft Matter* **7**, 5648 (2011).
- [9] A. Huerre, O. Theodoly, A. M. Leshansky, M.-P. Valignat, I. Cantat, and M.-C. Jullien, Droplets in Microchannels: Dynamical Properties of the Lubrication Film, *Phys. Rev. Lett.* **115**, 064501 (2015).
- [10] M. Yahashi, N. Kimoto, and K. Okumura, Scaling crossover in thin-film drag dynamics of fluid drops in the Hele-Shaw cell, *Sci. Rep.* **6**, 31395 (2016).
- [11] L. Keiser, K. Jaafar, J. Bico, and E. Reyssat, Dynamics of non-wetting drops confined in a Hele-Shaw cell, *J. Fluid Mech.* **845**, 245 (2018).
- [12] B. Reichert, A. Huerre, O. Theodoly, M.-P. Valignat, I. Cantat, and M.-C. Jullien, Topography of the lubrication film under a pancake droplet travelling in a Hele-Shaw cell, *J. Fluid Mech.* **850**, 708 (2018).
- [13] I. Shukla, N. Kofman, G. Balestra, L. Zhu, and F. Gallaire, Film thickness distribution in gravity-driven pancake-shaped droplets rising in a Hele-Shaw cell, *J. Fluid Mech.* **874**, 1021 (2019).
- [14] G. M. Homsy, Viscous fingering in porous media, *Annu. Rev. Fluid Mech.* **19**, 271 (1987).
- [15] L. Zhu and F. Gallaire, A pancake droplet translating in a {Hele-Shaw} cell: lubrication film and flow field, *J. Fluid Mech.* **798**, 955 (2016).
- [16] J. W. M. Bush, The anomalous wake accompanying bubbles rising in a thin gap: A mechanically forced Marangoni flow, *J. Fluid Mech.* **352**, 283 (1997).
- [17] F. Gallaire, P. Meliga, P. Laure, and C. N. Baroud, Marangoni induced force on a drop in a Hele-Shaw cell, *Phys. Fluids* **26**, 062105 (2014).
- [18] N. R. Gupta, A. Nadim, H. Haj-Hariri, and A. Borhan, On the linear stability of a circular drop translating in a hele-shaw cell, *J. Colloid Interface Sci.* **218**, 338 (1999).
- [19] N. R. Gupta, A. Nadim, H. Haj-Hariri, and A. Borhan, Stability of the shape of a viscous drop under buoyancy-driven translation in a hele-shaw cell, *J. Colloid Interface Sci.* **222**, 107 (2000).
- [20] N. R. Gupta, A. Nadim, H. Haj-Hariri, and A. Borhan, A numerical study of the effect of insoluble surfactants on the stability of a viscous drop translating in a hele-shaw cell, *J. Colloid Interface Sci.* **252**, 236 (2002).
- [21] E. Lajeunesse, J. Martin, N. Rakotomalala, and D. Salin, 3D Instability of Miscible Displacements in a Hele-Shaw Cell, *Phys. Rev. Lett.* **79**, 5254 (1997).
- [22] E. Lajeunesse, J. Martin, N. Rakotomalala, D. Salin, and Y. C. Yortsos, Miscible displacement in a Hele-Shaw cell at high rates, *J. Fluid Mech.* **398**, 299 (1999).



- [23] P. Petitjeans, C.-Y. Chen, E. Meiburg, and T. Maxworthy, Miscible quarter five-spot displacements in a Hele-Shaw cell and the role of flow-induced dispersion, *Phys. Fluids* **11**, 1705 (1999).
- [24] M. Kojima, E. J. Hinch, and A. Acrivos, The formation and expansion of a toroidal drop moving in a viscous fluid, *Phys. Fluids* **27**, 19 (1984).
- [25] F. T. Arecchi, P. K. Buah-Bassuah, and C. Perez-Garcia, Fragment formation in the break-up of a drop falling in a miscible liquid, *Europhys. Lett.* **15**, 429 (1991).
- [26] F. T. Arecchi, P. K. Buah-Bassuah, F. Francini, and S. Residori, Fragmentation of a drop as it falls in a lighter miscible fluid, *Phys. Rev. E* **54**, 424 (1996).
- [27] S. Residori, P. K. Buah-Bassuah, and F. T. Arecchi, Fragmentation instabilities of a drop as it falls in a miscible fluid, *Eur. Phys. J.: Spec. Top.* **146**, 357 (2007).
- [28] M. Shimokawa, R. Mayumi, T. Nakamura, T. Takami, and H. Sakaguchi, Breakup and deformation of a droplet falling in a miscible solution, *Phys. Rev. E* **93**, 062214 (2016).
- [29] N. Baumann, D. D. Joseph, P. Mohr, and Y. Renardy, Vortex rings of one fluid in another in free fall, *Phys. Fluids A* **4**, 567 (1992).
- [30] Thomson, On the formation of vortex rings by drops falling into liquids, and some allied phenomena, *Proc. R. Soc. London* **39**, 417 (1886).
- [31] F. T. Arecchi, P. K. Buah-Bassuah, F. Francini, C. Pérez-Garcia, and F. Quercioli, An experimental investigation of the break-up of a liquid drop falling in a miscible fluid, *Europhys. Lett.* **9**, 333 (1989).
- [32] M. Shimokawa and H. Sakaguchi, Mode selection on breakup of a droplet falling into a miscible solution, *Phys. Rev. Fluids* **4**, 013603 (2019).
- [33] G. Taylor and P. G. Saffman, A note on the motion of bubbles in a Hele-Shaw cell and porous medium, *Q. J. Mech. Appl. Math.* **12**, 265 (1959).
- [34] N. Joukowsky, Über die konturen der Tragflächen der Drachenflieger, *Z. Flugtech. Motorluftschiffahrt* **1**, 281 (1910).
- [35] D. Obaton and D. J. Tritton, Measurement of the thickness of a fluid layer by light absorption, *Exp. Fluids* **16**, 349 (1994).
- [36] E. Lajeunesse, J. Martin, N. Rakotomalala, D. Salin, and Y. C. Yortsos, The threshold of the instability in miscible displacements in a Hele-Shaw cell at high rates, *Phys. Fluids* **13**, 799 (2001).
- [37] C. Jiao and T. Maxworthy, An experimental study of miscible displacement with gravity-override and viscosity-contrast in a Hele-Shaw cell, *Exp. Fluids* **44**, 781 (2008).
- [38] See Supplemental Material at <http://link.aps.org/supplemental/10.1103/PhysRevFluids.6.103601> for movies of the drops presented in Fig. 9(a).